











Structural properties, morphology, total conductivity and oxygen mobility of composite materials based on Bi cerates

Nikita Ereemeev ^{a*} , Semyon Mironov ^a , Ekaterina Sadovskaya ^a , Tamara Krieger ^a , Arcady Ishchenko ^a , Artyom Ulikhin ^b , Vladislav Sadykov ^a , Yulia Bepalko ^a 

a: Federal Research Center Boreskov Institute of Catalysis SB RAS , Novosibirsk 630090, Russia

b: Institute of Solid State Chemistry and Mechanochemistry SB RAS , Novosibirsk 630128, Russia

* Corresponding author: yeremeev21@catalysis.ru

Abstract

Search of the new composite materials with mixed oxide-ionic–electronic conductivity and studies of their characteristics are important problems in the development of oxygen separation membranes as parts of catalytic reactors for biofuel transformation into syngas. Such composites are generally based on complex oxides with perovskite, fluorite, pyrochlore structure, etc. In this work, composites based on Bi cerates, Y-doped ceria and Pr nickelate-cobaltite are synthesized and studied. The composites are synthesized via ultrasonic dispersion in isopropanol. The obtained materials are characterized by X-ray diffraction, scanning and high resolution transmission electron microscopy. Electrical conductivity of the composites is studied by impedance spectroscopy. Oxygen transport properties are investigated by isotope exchange of oxygen with C¹⁸O₂ in a flow reactor. The samples are comprised of fluorite, perovskite and, sometimes, pyrochlore phases and various admixtures with different compositions, apparently, due to cation redistribution and solid state reactions between phases. The total conductivity of samples is ~10⁻¹ S/cm at 600 °C, which is high enough for using in the oxygen separation membranes. According to the isotope exchange data, the samples possess high oxygen mobility and surface reactivity. There is a distinct nonuniformity in the oxygen mobility, which is related to the effect of fast diffusion of oxygen associated with Bi and Ce cations, as well as the features of phase composition and real/defect structure. This makes the composites studied promising for using in the oxygen separation membranes.

Key findings

- The composites based on Bi_{2-x}Y_xCe₂O_{7-δ}, Ce_{0.9}Y_{0.1}O_{2-δ} and PrNi_{0.5}Co_{0.5}O_{3-δ} are synthesized for the first time.
- The main phases are fluorite and perovskite; various extended defects are observed.
- The total conductivity of the composites is high enough for using in oxygen separation membranes.
- Very high oxygen mobility ($D^* \sim 10^{-8}$ cm²/s at 400 °C) and surface reactivity is shown even at low temperatures.
- Various oxygen forms differing in mobility can be associated with the phase composition, extended defects, and developed interfaces.

© 2025, the Authors. This article is published in open access under the terms and conditions of the Creative Commons Attribution (CC BY) license (<http://creativecommons.org/licenses/by/4.0/>).

1. Introduction

Oxygen separation membranes are devices which are selectively permeable with respect to oxygen due to coupled transport of oxygen anions/vacancies and electrons/holes. Such membranes have been used for pure oxygen production, transformation of hydrocarbons, oxygenates and oth-

er fuels into syngas and other applications in energy, petrochemical industry, medicine, etc. [1–4]. Conventional oxygen separation membrane materials such as Sr-doped La ferrites-nickelates/cobaltites (LSFN, LSFC) and Sr-doped Ba ferrites-cobaltites (BSFC) possessed high mixed ionic-electronic conductivity, providing high oxygen permeation fluxes; however, they demonstrate a lack of stability in



Accompanying information

Article history

Received: 04.09.25

Revised: 01.10.25

Accepted: 06.10.25

Available online: 10.10.25

Keywords

fluorites; Bi cerates; composites; impedance spectroscopy; isotope heteroexchange; oxygen mobility

Funding

This work was supported by the Russian Science Foundation (Project No. [23-73-00045](https://doi.org/10.2373-73-00045)).

Supplementary information

Transparent peer review: 

Sustainable Development Goals



CH₄, CO and CO₂-containing atmospheres due to nature of alkaline earth elements and variable charge of B-site cations. Such approaches as optimizing composition, synthesis techniques and treatment conditions resulted in improving stability [5–8]. An alternative approach consists in developing and studying the other types of materials with mixed ionic-electronic conductivity for the oxygen separation membranes.

Oxides and solid solutions based on fluorites and pyrochlores, their derivatives, as well as their composites are considered candidate materials for the oxygen separation membranes due to their transport features [9–15]. Fluorites and pyrochlores can possess pure ionic (oxide-ionic and/or protonic) or mixed ionic-electronic conductivity depending on their composition.

There has been an interest in composites based on Ce–Bi–M–O (M – various transition, rare-earth and other elements) solid solutions, which can have fluorite, pyrochlore and other structures depending on the composition and synthesis conditions. This is due to Bi₂O₃-based materials possessing a high oxide-ionic conductivity and reducibility [16–18], and the effect of the presence of Bi³⁺ cations in the cationic sublattice of the solid solution structure on the structural defects, disorder and oxygen vacancy content [19–21], as well as the other oxygen transport features inherent in the respective structure types such as various migration mechanisms [14,22–26] and the effect of grain boundaries [27–30], which would allow to reach high oxygen permeation fluxes. For undoped Bi₂Ce₂O₇ the pyrochlore structure was found to be unstable at high temperatures due to a low Bi/Ce cations size ratio ($r_{\text{Bi}^{3+_{\text{VIII}}}}/r_{\text{Ce}^{4+_{\text{VI}}}} = 1.39$, which is outside of the stability ratio of 1.46–1.78) [31], thus tending to form a defective fluorite structure where Bi and Ce cations are randomly distributed in CeO₂-like lattice [16,32]. The doping with smaller Y cations [31] was shown to obtain stable solid solutions while maintaining high oxide-ionic conductivity values [33,34]. Unfortunately, the transport properties of Bi cerates still have not been studied well. On the other hand, due to redox activity of Ce^{4+/3+} cations Bi cerates possess a high oxygen mobility [19,35–37], which was experimentally demonstrated in the authors' previous work [38].

Unfortunately, fluorites and pyrochlores do not always have high electronic conductivity which, along with oxide-ionic conductivity, is necessary for the oxygen separation membranes as well. Using dual- and triple-phased composites is a promising approach [1,2,4–10,13,39]. PrNi_{0.5}Co_{0.3}O_{3-δ} as well as their composites with Ce_{0.9}Y_{0.1}O_{2-δ} demonstrate a high total conductivity, oxygen mobility and surface reactivity, and the asymmetric supported membranes with permselective layer based on such a composite show high oxygen permeation fluxes and good performance in catalytic reactions with oxygen as a reagent [6,40,41]. Consequently, the assessment of phase composition, total and oxide-ionic conductivity of composites based on Bi cerates, fast oxide-ionic conductors,

PrNi_{0.5}Co_{0.3}O_{3-δ} and Ce_{0.9}Y_{0.1}O_{2-δ} is a subject of considerable interest.

In this work, the structural, morphological and oxygen transport properties, and total conductivity of Bi_{2-x}Y_xCe₂O_{7-δ} (x = 0.0, 0.4) – Ce_{0.9}Y_{0.1}O_{2-δ} and Bi_{2-x}Y_xM₂O_{7-δ} – Ce_{0.9}Y_{0.1}O_{2-δ} – PrNi_{0.5}Co_{0.5}O_{3-δ} composites were studied. The composites were synthesized via ultrasonic dispersion. Oxygen diffusion features were studied using temperature-programmed isotope exchange of oxygen with C¹⁸O₂ in a flow reactor.

2. Materials and methods

2.1. Synthesis of materials

As initial materials, Bi₂Ce₂O_{7-δ} (BC), Bi_{1.6}Y_{0.4}Ce₂O_{7-δ} (BYC), Ce_{0.9}Y_{0.1}O_{2-δ} (YDC) and PrNi_{0.5}Co_{0.5}O_{3-δ} (PNC) powders synthesized by the Pechini technique as described elsewhere [39,42] were used. The following reagents were utilized as starting materials: Bi(NO₃)₃·5H₂O (>99 %), Ce(NO₃)₃·6H₂O (>99 %), Y(NO₃)₃·6H₂O (>99 %), Pr(NO₃)₃·6H₂O (>99 %), Ni(NO₃)₂·6H₂O (>99 %), and Co(NO₃)₂·6H₂O (>99 %). The nitrates were mixed in the corresponding stoichiometric ratio and dissolved in distilled water. Citric acid was dissolved in ethylene glycol. Subsequently, a nitrate aqueous solution was mixed with a citric acid ethylene glycol solution, followed by the addition of ethylene diamine. The molar ratio of total metal nitrates: citric acid: ethylene diamine: ethylene glycol was 1:3.75:3.75:11.25. The xerogels obtained were dried in a drying oven at 80 °C for 12 h, then calcined at 500 °C for 3 h.

BC–YDC (Bi₂Ce₂O_{7-δ} (50 wt. %) – Ce_{0.9}Y_{0.1}O_{2-δ}), BYC–YDC (Bi_{1.6}Y_{0.4}Ce₂O_{7-δ} (50 wt. %) – Ce_{0.9}Y_{0.1}O_{2-δ}), BC–YDC–PNC (Bi₂Ce₂O_{7-δ} (30 wt. %) – Ce_{0.9}Y_{0.1}O_{2-δ} (30 wt. %) – PrNi_{0.5}Co_{0.5}O_{3-δ}) and BYC–YDC–PNC (Bi_{1.6}Y_{0.4}Ce₂O_{7-δ} (30 wt. %) – Ce_{0.9}Y_{0.1}O_{2-δ} (30 wt. %) – PrNi_{0.5}Co_{0.5}O_{3-δ}) composites were synthesized by an ultrasonic dispersion technique using the as-prepared BC, BYC, YDC and PNC powders in the respective weight ratios. A mixture of the oxides was dispersed in isopropanol with addition of polyvinyl butyral for 40 min using IKA RW 14 Basic (Germany) homogenizer, then dried at 80 °C for 2 h and calcined at 500 °C for 2 h.

The powders of the composites were pelletized and sintered at 700 °C for 3 h, at 900 °C for 3 h, and at 1100 °C for 10 h in a furnace in air.

2.2. Characterization of materials

The phase composition of the materials obtained was studied by the X-ray diffraction (XRD) using a Bruker D8 Advance diffractometer with the Lynx-Eye detector using Cu Kα radiation. XRD patterns were recorded in the 2θ range of 15–95° with a step of 0.05°.

SEM images were obtained using FIB-SEM microscope (Tescan Solaris, Brno-Kohoutovice, Czech Republic) equipped with secondary and reflected electron detectors.

The studies of materials by high resolution transmission electron microscopy (HR TEM) were carried out using JEM-2010 and JEM-2200FS (JEOL Ltd., Japan) electron microscopes. The accelerating voltage was 200 kV, the resolution was 1.4 Å. Local analysis of elemental composition of the samples was carried out by EDX analysis using a Phoenix spectrometer with Si(Li) detector and energy resolution not exceeding 130 eV.

2.3. Total conductivity studies

The composites were studied by the electrochemical impedance spectroscopy (EIS) technique in two-electrode cells with Ag electrodes using 4284A (Agilent/HP) precision LCR meter in the alternating current frequency range of 20 Hz - 1 MHz at temperatures of 200–600 °C. Total bulk electrical conductivity values were determined by analyzing $Z'' = f(Z')$ Nyquist plots.

2.4. Oxygen diffusivity studies

The oxygen tracer diffusion coefficient (D^*) and surface heteroexchange rate (R) values of the samples were acquired using the temperature-programmed isotope exchange of oxygen (TPIE) with $C^{18}O_2$ in a flow reactor. The samples (fraction 0.25–0.5 mm) were loaded into a quartz reactor with an inner diameter of 3 mm. The pretreatment was carried out in the flow of 1% $O_2 + He$ (flow rate of 25 ml/min) at 700 °C for 0.5 h. The TPIE experiments were performed while heating from 50 °C to 800 °C with a ramp of 5 °C/min in the flow of 1% $C^{18}O_2 + 1\% Ar + He$ (flow rate of 25 ml/min). The composition of the gas mixture in the reactor outlet was monitored by the SRS UGA 200 (Stanford Research Systems, USA) mass spectrometer. The curves of ^{18}O atomic fraction (α) and $C^{16}O^{18}O$ molecular fraction (f_{16-18}) were used for analysis of the isotopic response in order to calculate the oxygen tracer diffusion coefficient (D^*), surface heteroexchange rate (R) and their effective activation energy (E_D, E_R). The error in the calculation of D^* , R , E_D and E_R values did not exceed $\pm 15\%$.

3. Results and Discussion

3.1. Structural features

According to the XRD data (Figure 1), the composites BC-YDC and BC-YDC-PNC sintered at 700 °C does not demonstrate the formation of new phases corresponding to chemical interaction of the initial BC [38], YDC [41] and PNC [41] components. For the BC-YDC sample sintered at 1100 °C, Bi cerate transforms into the mixture of fluorite-like oxides corresponding to CeO_2 and Bi_3YO_6 [PDF 026-0229]. Similar tendencies are observed for BYC-YDC composites (Figure 2). After sintering at 1100 °C, for BC-YDC-PNC and BYC-YDC-PNC samples, the perovskite phase is partially preserved, NiO phase emerges, and two fluorite-like phase corresponding to CeO_2 and Bi_3YO_6 are present (Figures 1, 2).

3.2. Morphology

According to the SEM data for the pellets (Figures 3 and 4), the samples are not sintered well after sintering at 900 °C, and the subsequent sintering at 1100 °C allows obtaining dense samples. Studying the composites sintered at 1100 °C by the HR TEM technique demonstrates uniform element distribution and presence of clear interfaces (Figures 5–7). The individual particles of the composites are nanosized and well-crystallized (Figure 6, left images). Defects such as lattice strains, grain boundaries and stacking faults are visible in the HR TEM images. Low-contrast regions observed on the surface of some nanoparticles may suggest the presence of highly-defective or even partially amorphous layers.

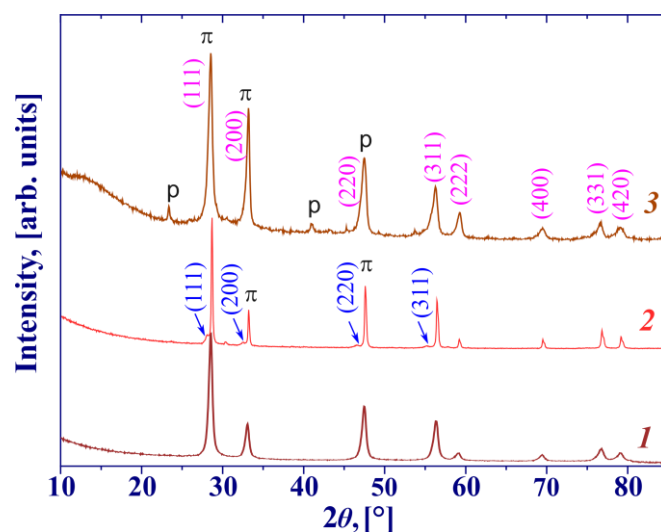


Figure 1 XRD patterns for $Bi_2Ce_2O_{7-\delta}$ (50 wt.%) - $Ce_{0.9}Y_{0.1}O_{2-\delta}$ samples sintered at 700 °C (1) and 1100 °C (2), and $Bi_2Ce_2O_{7-\delta}$ (30 wt.%) - $Ce_{0.9}Y_{0.1}O_{2-\delta}$ (30 wt.%) - $PrNi_{0.5}Co_{0.5}O_{3-\delta}$ sample sintered at 700 °C (3). Phases: magenta hkl indices - fluorite, blue hkl indices - Bi_3YO_6 , π - pyrochlore, p - perovskite.

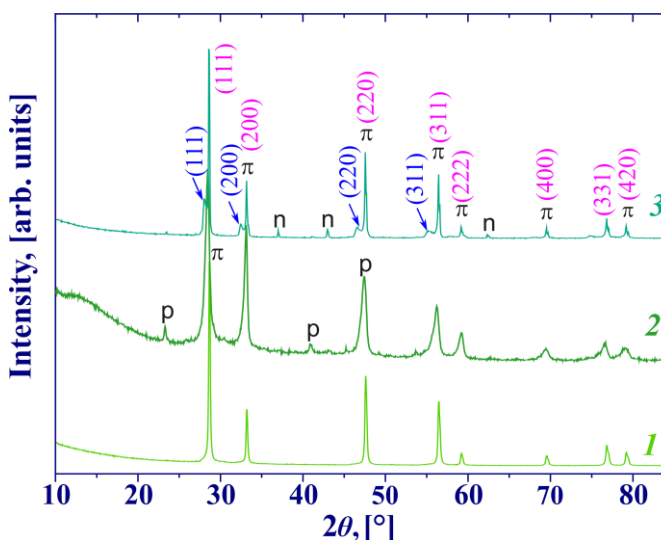


Figure 2 XRD patterns for $Bi_{1.6}Y_{0.4}Ce_2O_{7-\delta}$ (50 wt.%) - $Ce_{0.9}Y_{0.1}O_{2-\delta}$ sample sintered at 1100 °C (1) and $Bi_{1.6}Y_{0.4}Ce_2O_{7-\delta}$ (30 wt.%) - $Ce_{0.9}Y_{0.1}O_{2-\delta}$ (30 wt.%) - $PrNi_{0.5}Co_{0.5}O_{3-\delta}$ samples sintered at 700 °C (2) and 1100 °C (3). Phases: magenta hkl indices - fluorite, blue hkl indices - Bi_3YO_6 , π - pyrochlore, p - perovskite, n - NiO.

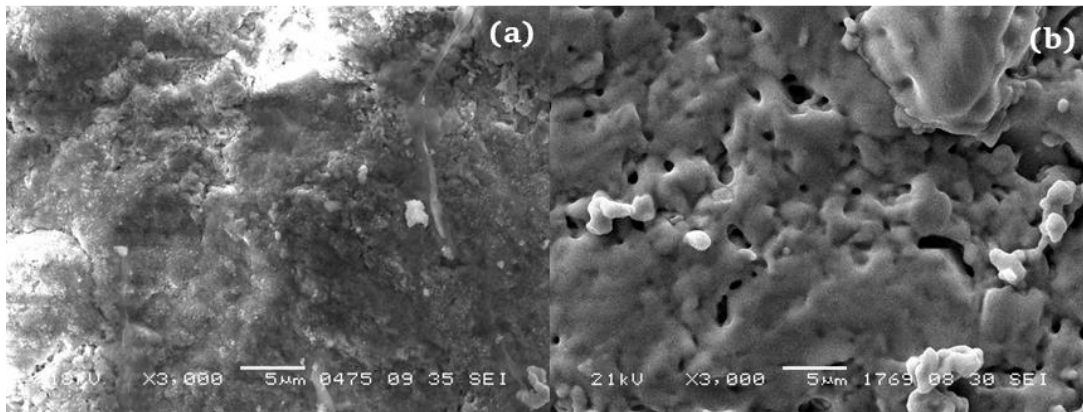


Figure 3 SEM images of $\text{Bi}_{1.6}\text{Y}_{0.4}\text{Ce}_2\text{O}_{7-\delta}$ (50 wt.%) - $\text{Ce}_{0.9}\text{Y}_{0.1}\text{O}_{2-\delta}$ samples sintered at 900 °C (a) and 1100 °C (b).

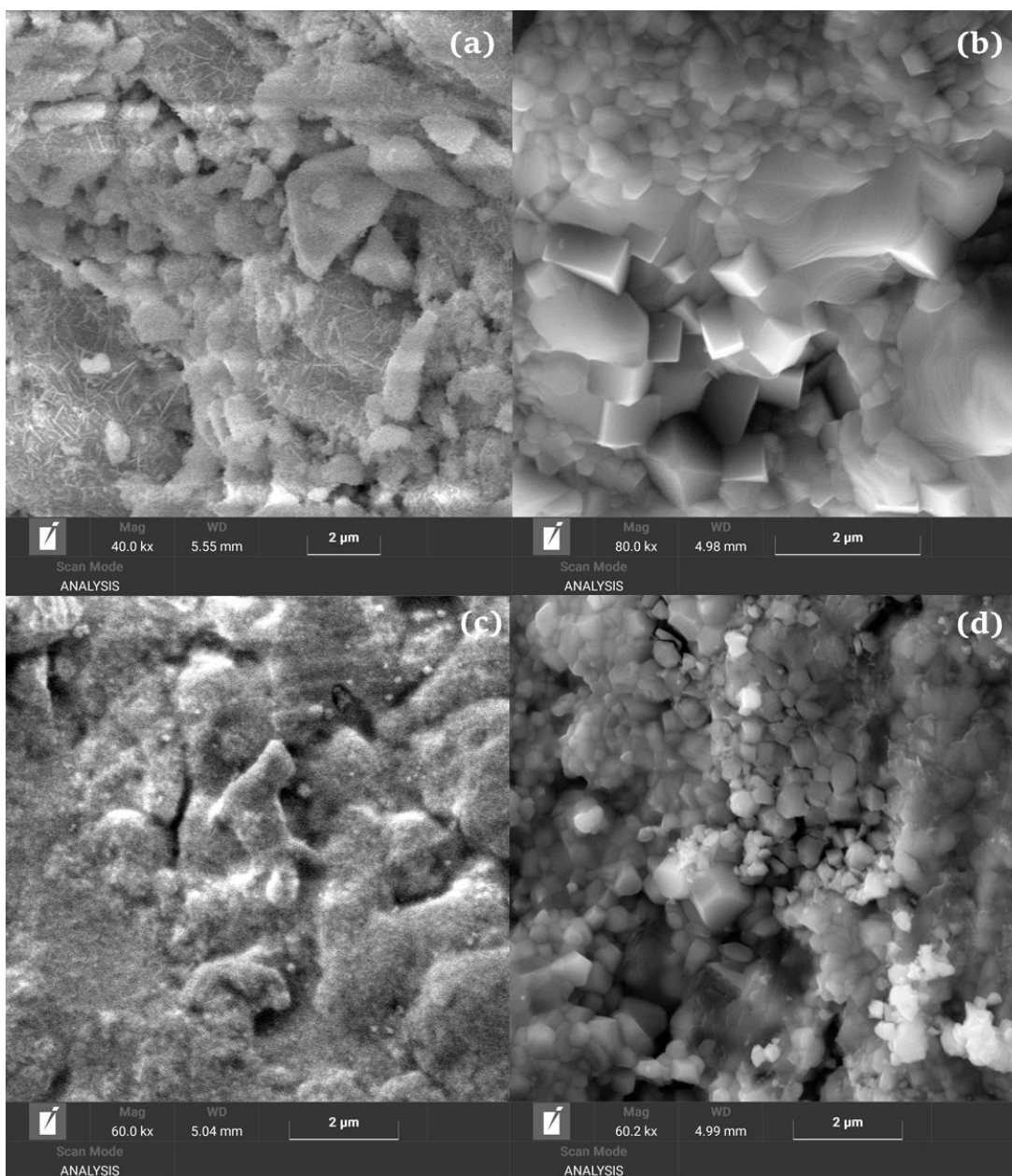


Figure 4 SEM images of $\text{Bi}_2\text{Ce}_2\text{O}_{7-\delta}$ (50 wt.%) - $\text{Ce}_{0.9}\text{Y}_{0.1}\text{O}_{2-\delta}$ (a) $\text{Bi}_2\text{Ce}_2\text{O}_{7-\delta}$ (30 wt.%) - $\text{Ce}_{0.9}\text{Y}_{0.1}\text{O}_{2-\delta}$ (30 wt.%) - $\text{PrNi}_{0.5}\text{Co}_{0.5}\text{O}_{3-\delta}$ (b), $\text{Bi}_{1.6}\text{Y}_{0.4}\text{Ce}_2\text{O}_{7-\delta}$ (50 wt.%) - $\text{Ce}_{0.9}\text{Y}_{0.1}\text{O}_{2-\delta}$ (c) and $\text{Bi}_{1.6}\text{Y}_{0.4}\text{Ce}_2\text{O}_{7-\delta}$ (30 wt.%) - $\text{Ce}_{0.9}\text{Y}_{0.1}\text{O}_{2-\delta}$ (30 wt.%) - $\text{PrNi}_{0.5}\text{Co}_{0.5}\text{O}_{3-\delta}$ (c, d) sintered at 1100 °C.

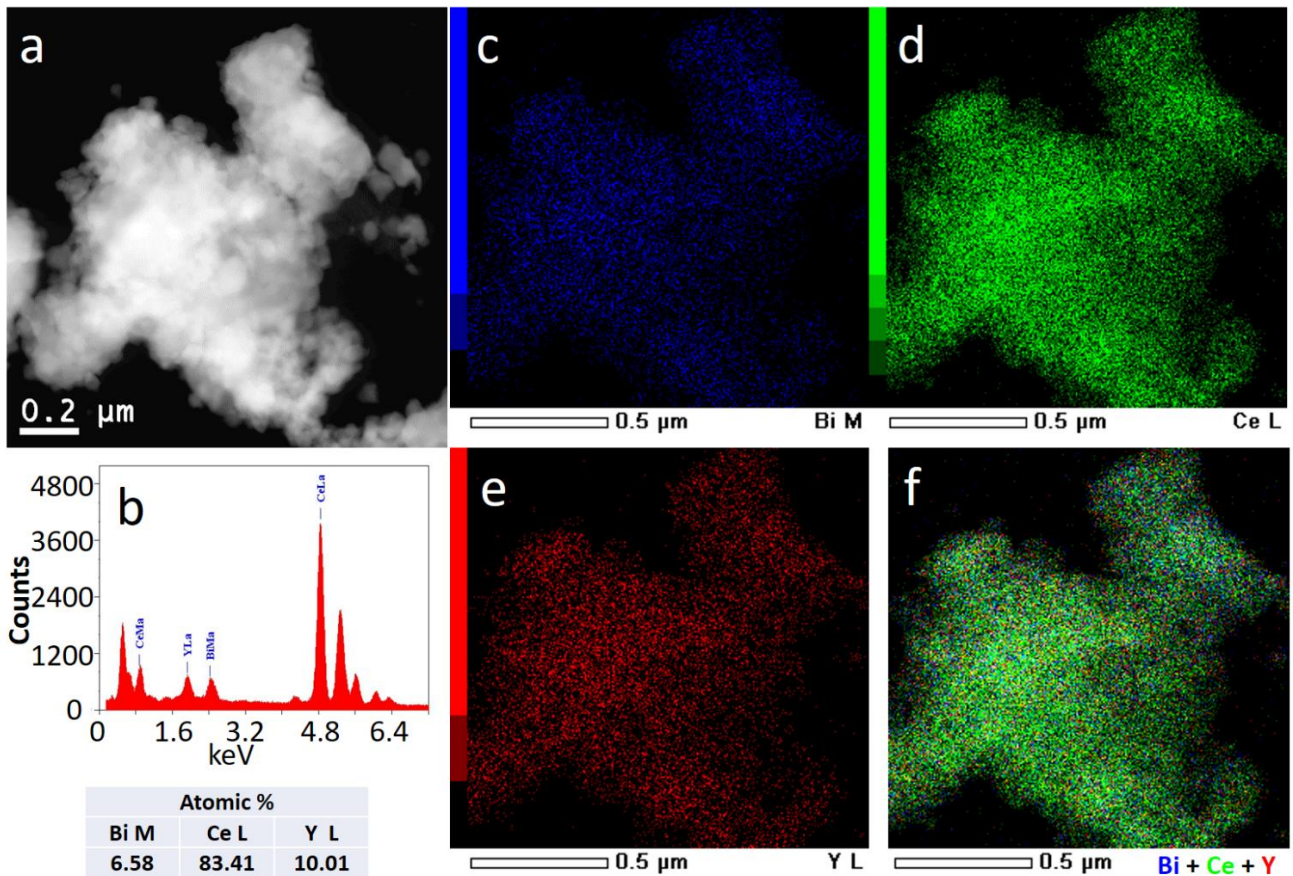


Figure 5 HAADF STEM image (a), EDX spectrum from the corresponding area (b) with the composition calculation table, mapping by characteristic lines of elements Bi-M (c), Ce-L (d), Y-L (e) and layered image (f) for the $\text{Bi}_2\text{Ce}_2\text{O}_{7-\delta}$ (50 wt. %) - $\text{Ce}_{0.9}\text{Y}_{0.1}\text{O}_{2-\delta}$ sample sintered at 1100 °C.

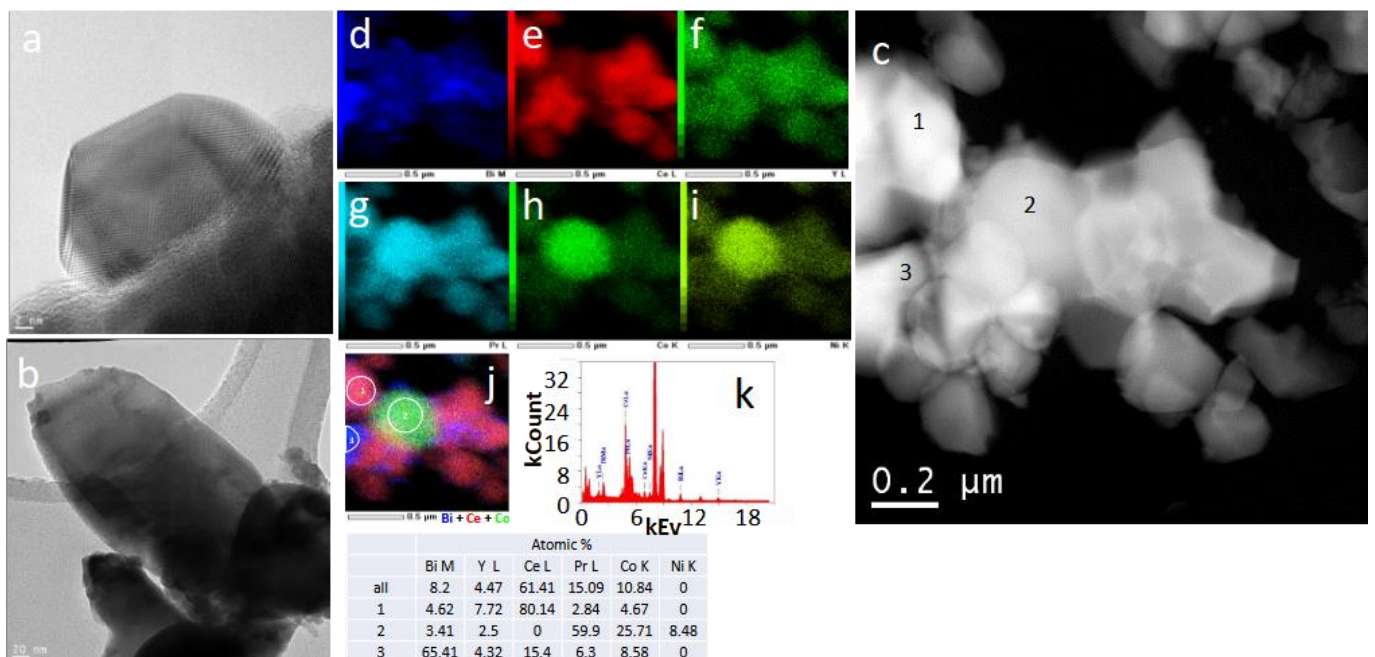


Figure 6 HRTEM (a), TEM (b) images; HAADF STEM image (c), mapping by characteristic lines of elements Bi-M (d), Ce-L (e), Y-L (f) Pr-L (g), Co-K (h), Ni-K (i), layered {Bi+Ce+Co} image (j) and EDX spectrum from the corresponding area (k) with the composition calculation table for the $\text{Bi}_2\text{Ce}_2\text{O}_{7-\delta}$ (30 wt. %) - $\text{Ce}_{0.9}\text{Y}_{0.1}\text{O}_{2-\delta}$ (30 wt. %) - $\text{PrNi}_{0.5}\text{Co}_{0.5}\text{O}_{3-\delta}$ sample sintered at 1100 °C.

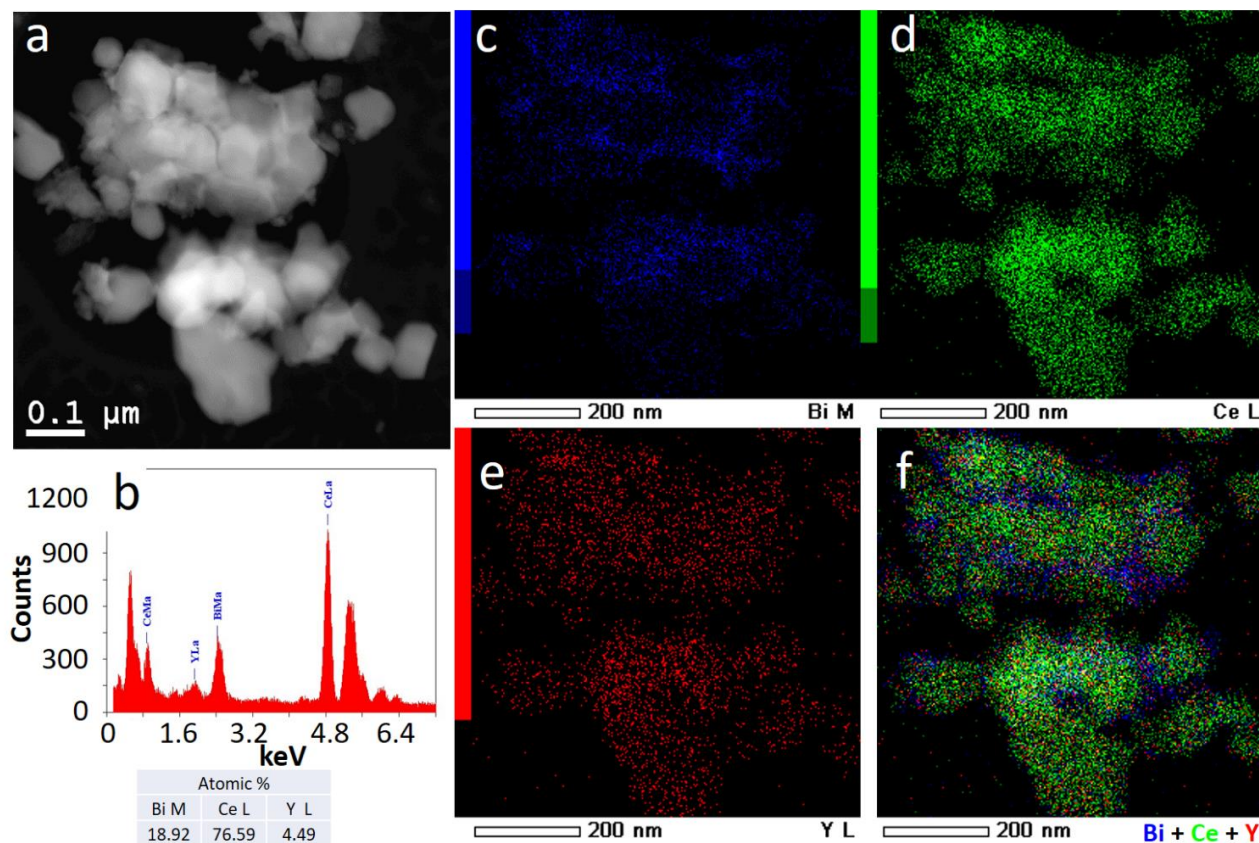


Figure 7 HAADF STEM image (a), EDX spectrum from the corresponding area (b) with the composition calculation table, mapping by characteristic lines of elements Bi-M (c), Ce-L (d), Y-L (e) and layered image (f) for the $\text{Bi}_{1.6}\text{Y}_{0.4}\text{Ce}_2\text{O}_{7-\delta}$ (50 wt. %) - $\text{Ce}_{0.9}\text{Y}_{0.1}\text{O}_{2-\delta}$ sample sintered at 1100°C .

Such defect and morphological features may affect the oxygen transport properties facilitating the surface exchange and providing fast diffusion pathways.

3.3. Total conductivity

According to EIS measurements for the triple-component composite samples sintered at 1100°C , the total conductivity values are $\sim 10^{-1}$ S/cm at 600°C (Figure 8) which can be considered as intermediate; however, this value is high enough for using in oxygen separation membranes [6,32,35]. Total conductivity values of Bi cerate-based composites are higher compared to those acquired for individual Bi cerates [19,32,36,37]. Doping with Y leads to increase in total conductivity of Bi cerate based composites by about a half order of magnitude. The effective activation energy values are almost independent of temperature within the range of $200\text{--}600^\circ\text{C}$ and are ~ 50 kJ/mol for the BC-YDC-PNC and BYC-YDC-PNC samples. The effective activation energy values for the composites are lower compared to those for $\text{CeO}_2\text{-Bi}_2\text{O}_3$ solid solutions [19,36,37]; however, they are higher compared to those for PNC and PNC-YDC composites [41].

3.4. Oxygen mobility and surface reactivity

Figure 9 illustrates the temperature dependences of the ^{18}O atomic fraction in CO_2 for the BC and BYC samples sintered at 700°C acquired during TPIE C^{18}O_2 in the flow

reactor [38]. For both samples, a weak peak with an extremum at approximately 80°C and a main peak with an extremum at approximately 150°C are observed. The first peak is associated with the isotope exchange of surface oxygen in the samples, while the second peak is linked to the isotopic substitution of oxygen within the sample bulk. The main $\alpha(T)$ peak is observed to be considerably asymmetric with respect to the extremum for both samples. This indicates that the oxygen within the sample bulk exhibits significant nonuniformity in its capacity for isotopic substitution.

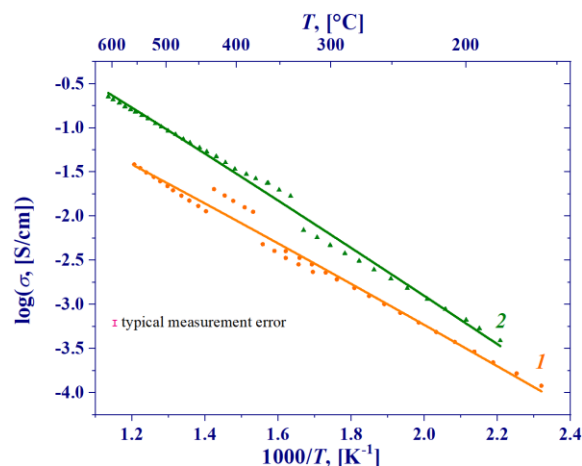


Figure 8 Total conductivity depending on the temperature for $\text{Bi}_2\text{Ce}_2\text{O}_{7-\delta}$ (30 wt.%) - $\text{Ce}_{0.9}\text{Y}_{0.1}\text{O}_{2-\delta}$ (30 wt.%) - $\text{PrNi}_{0.5}\text{Co}_{0.5}\text{O}_{3-\delta}$ (1) and $\text{Bi}_{1.6}\text{Y}_{0.4}\text{Ce}_2\text{O}_{7-\delta}$ (30 wt.%) - $\text{Ce}_{0.9}\text{Y}_{0.1}\text{O}_{2-\delta}$ (30 wt.%) - $\text{PrNi}_{0.5}\text{Co}_{0.5}\text{O}_{3-\delta}$ (2) samples sintered at 1100°C .

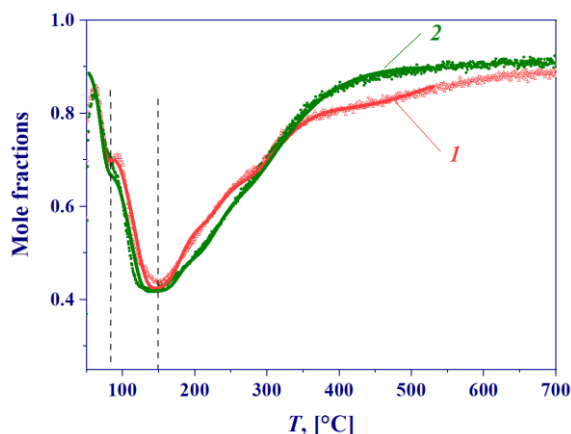


Figure 9 Temperature-programmed isotope exchange of oxygen with $C^{18}O_2$ in the flow reactor for the $Bi_2Ce_2O_{7-\delta}$ (1) and $Bi_{1.6}Y_{0.4}Ce_2O_{7-\delta}$ (2) samples sintered at 700 °C. Points – experiment, lines – modeling.

The numeric analysis within the framework of the model for the isotope exchange with oxides [43–45] reveals the presence of numerous forms of oxygen characterized by different tracer diffusion coefficient values in the structure of both samples. For the BC sample sintered at 700 °C, the effective activation energy of the most mobile form of oxygen (which constitutes approximately 60% of the total oxygen content in the oxide) is 110 kJ/mol, which is typical for numerous oxide systems [44–50]. The tracer diffusion coefficient for this form of oxygen is $\sim 10^{-6}$ cm²/s at 700 °C, which is atypically elevated and analogous to the values reported for Bi_2O_3 , a material known for its rapid oxide-ionic conduction [46,51,52], and the values documented for rapid diffusion along grain boundaries in certain oxides [53–55]. Regarding the rapid oxide-ionic conduction exhibited by Bi-containing oxides and the redox activity of Ce cations, it can be hypothesized that this fast form of oxygen likely corresponds to the oxide anions bound to Bi or Ce cations [35,38,56]. The substitution of the remaining oxygen is described by significantly lower tracer diffusion coefficient with very low effective activation energy of approximately 40 kJ/mol, which is atypical for oxides [46]. In this case, the calculated curve describing the high-temperature region is, in fact, an envelope of a number of overlapping peaks corresponding to the

forms of oxygen with different substitution rates. These forms of oxygen are probably more strongly bound oxide anions in the Bi cerate lattice [38].

For the BYC sample sintered at 700 °C, the diffusion coefficient of the most mobile oxygen fraction is nearly equivalent to that of the BC sample sintered at 700 °C; however, the substitution rate of the remaining oxygen fraction is significantly faster. Hence, doping with Y results in a more uniform oxygen mobility distribution among its different forms. Moreover, doping with Y may result in a higher content of oxygen vacancies as demonstrated for $Bi_{2-x}Y_xCe_2O_{7-\delta}$ ($x = 0-1.5$) in the work [56] which can explain increasing the diffusion coefficient values for the slow diffusion channel.

The calculated values of the oxygen surface exchange rate and tracer diffusion coefficient are provided in Table 1. The Arrhenius plots for oxygen tracer diffusion coefficients and surface heteroexchange rates (with $C^{18}O_2$) compared to the other materials [38,45,52,57–59] are given in Figure 10. It is worth to mention the exceptionally high values of the oxygen surface heteroexchange rate with $C^{18}O_2$ (Figure 10a, curves 1–3, 5). A fast oxygen surface heteroexchange rate can be associated with a presence of numerous extended defects on the sample surface as indicated by HR TEM (Figure 6). It was also reported that Bi–O–Ce species can form, and their oxygen can be easily transferred to the surface of the solid solution particles [20]. The oxygen vacancies in Bi-doped ceria can promote CO_2 molecule adsorption [60]. These factors are probably responsible for such high oxygen heteroexchange rates.

For the BYC–YDC composite sintered at 700 °C (Figure 11, curve 2), the substitution rate of the most mobile oxygen is nearly equivalent to that of the BYC sample (Figure 10b, curve 3); however, its fraction increases compared to the BYC sample reaching 70% (Table 1). Along with this, the substitution rate of the rest fraction of oxygen increases as well (Figure 10c, curve 3). It is to be noted that D^* values for the fast and slow diffusion channels exceed those for pure YDC [61], which may indicate a synergistic effect of BYC and YDC fluorites, as well as an effect of extended defects.

Table 1 The oxygen surface heteroexchange rates (R) and tracer diffusion coefficient (D^*) values at 500 K, their effective activation energies (E_R , E_D), and fraction of each oxygen form (θ_i) according to the TPIE $C^{18}O_2$ data modeling.

Sample (T_{sint} , [°C])	R , [s ⁻¹]	E_R , [kJ/mol]	D^*/L^2 (θ_i), [s ⁻¹]	D^* , [cm ² /s]	E_D , [kJ/mol]
BC (700)	$5 \cdot 10^5$	180	0.4 (60%) $1 \cdot 10^{-3}$	$3 \cdot 10^{-12}$ $7 \cdot 10^{-15}$	110 40
BYC (700)	$5 \cdot 10^5$	180	0.45 (60%) $1 \cdot 10^{-2}$	$3 \cdot 10^{-12}$ $7 \cdot 10^{-14}$	110 50
BYC–YDC (700)	$6 \cdot 10^5$	180	0.4 (70%) 0.1	$3 \cdot 10^{-12}$ $1 \cdot 10^{-12}$	110 80
BYC–YDC (1100)	Not det.		$1 \cdot 10^{-3}$	$4 \cdot 10^{-13}$	35
BYC–YDC–PNC (700)	$1 \cdot 10^5$	180	0.45 (60%) $1 \cdot 10^{-7}$	$1 \cdot 10^{-12}$ $3 \cdot 10^{-19}$	110 120
BYC–YDC–PNC (1100)	Not det.		$1.5 \cdot 10^{-3}$ (85%) $2 \cdot 10^{-10}$	$1 \cdot 10^{-12}$ $2 \cdot 10^{-19}$	45 140
YDC–PNC (1100)	Not det.		$3 \cdot 10^{-6}$ (70%) $5 \cdot 10^{-13}$	$8 \cdot 10^{-15}$ $1 \cdot 10^{-22}$	120 200

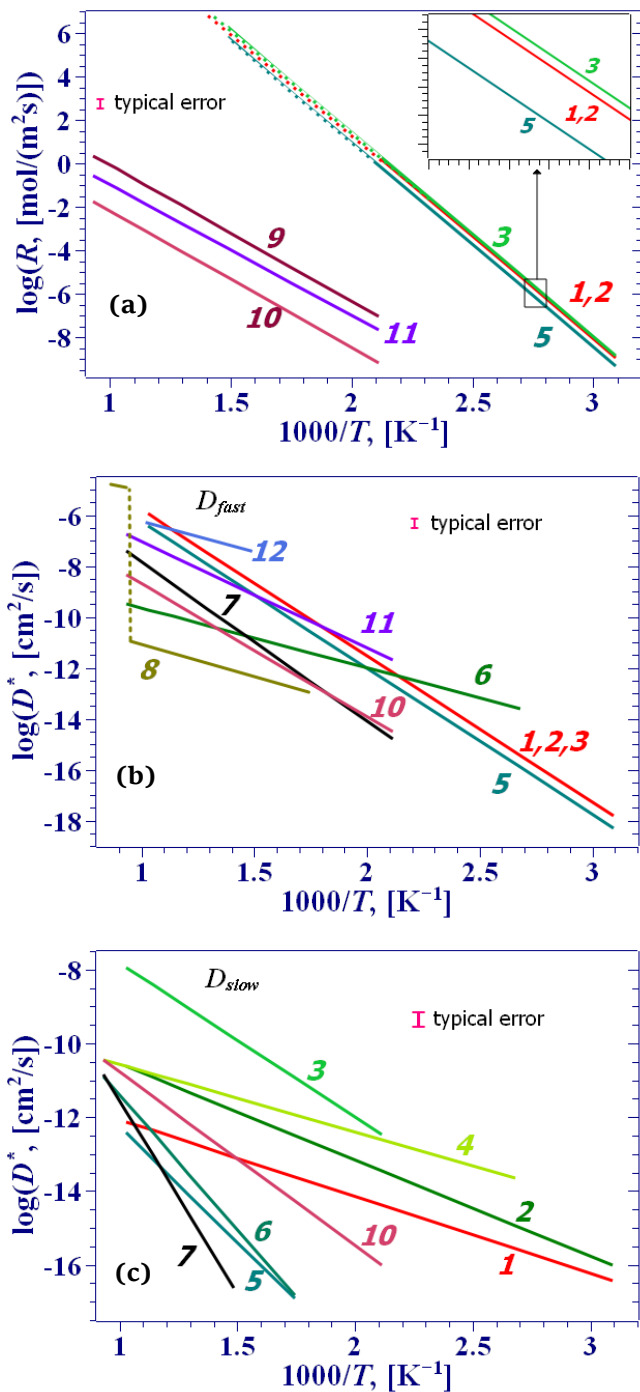


Figure 10 Arrhenius plots for the oxygen surface heteroexchange rate (a) and tracer diffusion coefficient for fast (b) and slow (c) diffusion channels for Bi cerate-based material compared to other oxide-ionic and mixed ionic-electronic conductors:

- (1) $\text{Bi}_2\text{Ce}_2\text{O}_{7-\delta}$ ($T_{\text{sint}} = 700$ °C) [38],
- (2) $\text{Bi}_{1.6}\text{Y}_{0.4}\text{Ce}_2\text{O}_{7-\delta}$ (700 °C) [38], (3) $\text{Bi}_2\text{Ce}_2\text{O}_{7-\delta}-\text{Ce}_{0.9}\text{Y}_{0.1}\text{O}_{2-\delta}$ (700 °C), (4) $\text{Bi}_2\text{Ce}_2\text{O}_{7-\delta}-\text{Ce}_{0.9}\text{Y}_{0.1}\text{O}_{2-\delta}$ (1100 °C),
- (5) $\text{Bi}_{1.6}\text{Y}_{0.4}\text{Ce}_2\text{O}_{7-\delta}-\text{Ce}_{0.9}\text{Y}_{0.1}\text{O}_{2-\delta}-\text{PrNi}_{0.5}\text{Co}_{0.5}\text{O}_{3-\delta}$ (700 °C),
- (6) $\text{Bi}_{1.6}\text{Y}_{0.4}\text{Ce}_2\text{O}_{7-\delta}-\text{Ce}_{0.9}\text{Y}_{0.1}\text{O}_{2-\delta}-\text{PrNi}_{0.5}\text{Co}_{0.5}\text{O}_{3-\delta}$ (1100 °C),
- (7) $\text{Ce}_{0.9}\text{Y}_{0.1}\text{O}_{2-\delta}-\text{PrNi}_{0.5}\text{Co}_{0.5}\text{O}_{3-\delta}$ (1100 °C) [45], (8) Bi_2O_3 [52],
- (9) $\text{La}_{1.6}\text{Sm}_{0.4}\text{NiO}_{4+\delta}$ [57]; (10) $\text{La}_{1.7}\text{Ca}_{0.3}\text{NiO}_{4+\delta}$ [58],
- (11) $\text{Pr}_2\text{NiO}_{4+\delta}$ [58], (12) $\text{Ba}_{0.5}\text{Sr}_{0.5}\text{Co}_{0.8}\text{Fe}_{0.2}\text{O}_{3-\delta}$ [59].

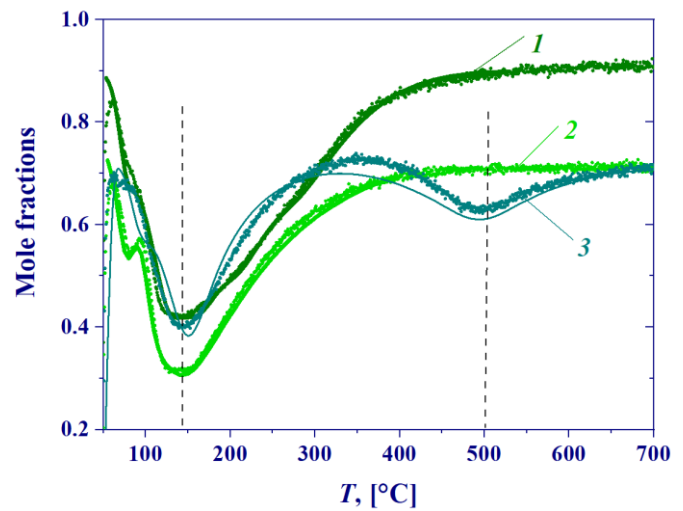


Figure 11 Temperature-programmed isotope exchange of oxygen with C^{18}O_2 in the flow reactor for the $\text{Bi}_{1.6}\text{Y}_{0.4}\text{Ce}_2\text{O}_{7-\delta}$ (1), $\text{Bi}_2\text{Ce}_2\text{O}_{7-\delta}-\text{Ce}_{0.9}\text{Y}_{0.1}\text{O}_{2-\delta}$ (2) and $\text{Bi}_{1.6}\text{Y}_{0.4}\text{Ce}_2\text{O}_{7-\delta}-\text{Ce}_{0.9}\text{Y}_{0.1}\text{O}_{2-\delta}-\text{PrNi}_{0.5}\text{Co}_{0.5}\text{O}_{3-\delta}$ (3) samples sintered at 700 °C. Points – experiment, lines – modeling.

For the BYC–YDC–PNC composite sintered at 700 °C, a second peak with an extremum at the temperature of approximately 500 °C emerges (Figure 11, curve 3), which is most likely associated with the PNC perovskite phase.

Increasing the sintering temperature up to 1100 °C results in a substantial decrease in the surface area, thereby extending the diffusion path. Consequently, the effective diffusion coefficient D^*/L^2 decreases leading to the shift of the TPIE peak related to the substitution of the bulk oxygen towards higher temperatures (Figures 12 and 13). The $\alpha(T)$ dependence for the BYC–YDC sample (Figure 12, curve 2) represents numerous of overlapping peaks with distinctly expressed local extrema associated with different oxygen forms. In this case, the mobility of these oxygen forms is not significantly different, and they can be described by a single diffusion coefficient with a low effective activation energy (Table 1). For the BYC–YDC–PNC sample sintered at 1100 °C, no local extrema in the region of the main TPIE peak are revealed (Figure 13, curve 2); however, a distinct broadening of the peak is observed, which suggests a higher degree of nonuniformity in the oxygen of the BYC–YDC–PNC sample sintered at 700 °C. The calculated diffusion parameters for the samples sintered at 1100 °C are given in Table 1. It is to be noted that the oxygen surface heteroexchange rate for these samples cannot be determined due to the low specific surface area.

A comparison of the TPIE data for the BYC–YDC–PNC sample sintered at 1100 °C with the data acquired during a similar experiment for the YDC–PNC sample sintered at 1100 °C (Figure 14) [42] reveals that the YDC–PNC sample exhibits enhanced structural integrity.

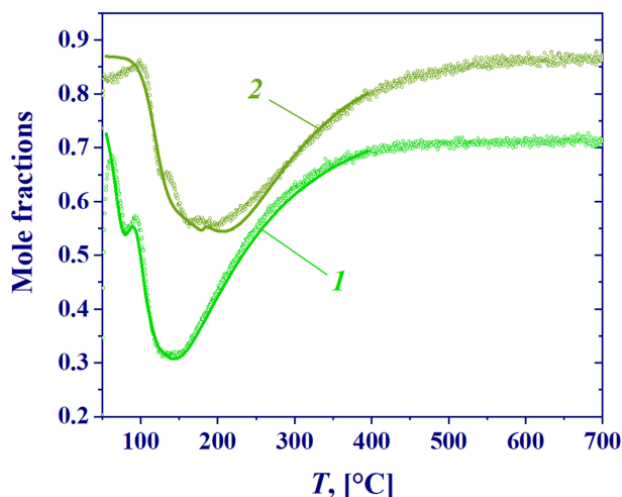


Figure 12 Temperature-programmed isotope exchange of oxygen with $C^{18}O_2$ in the flow reactor for the $Bi_{1.6}Y_{0.4}Ce_2O_{7-\delta}-Ce_{0.9}Y_{0.1}O_{2-\delta}$ samples sintered at 700 °C (1) and 1100 °C (2). Points - experiment, lines - modeling.

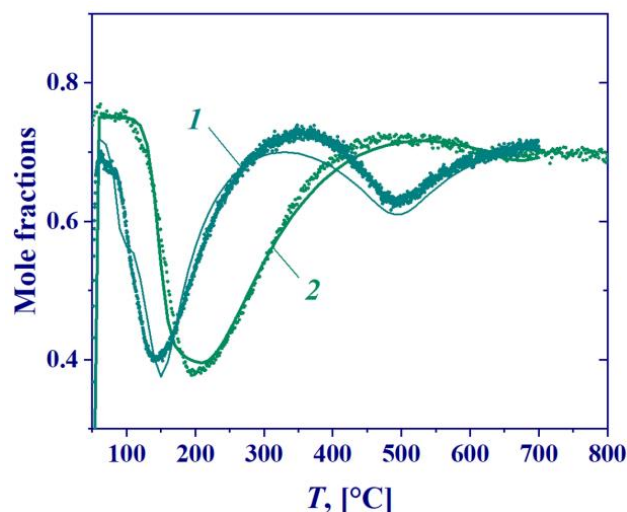


Figure 13 Temperature-programmed isotope exchange of oxygen with $C^{18}O_2$ in the flow reactor for the $Bi_{1.6}Y_{0.4}Ce_2O_{7-\delta}-Ce_{0.9}Y_{0.1}O_{2-\delta}-PrNi_{0.5}Co_{0.5}O_{3-\delta}$ samples sintered at 700 °C (1) and 1100 °C (2). Points - experiment, lines - modeling.

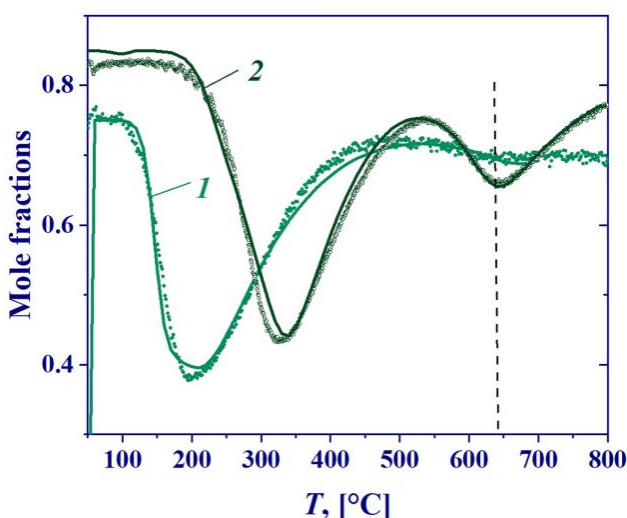


Figure 14 Temperature-programmed isotope exchange of oxygen with $C^{18}O_2$ in the flow reactor for the $Bi_{1.6}Y_{0.4}Ce_2O_{7-\delta}-Ce_{0.9}Y_{0.1}O_{2-\delta}-PrNi_{0.5}Co_{0.5}O_{3-\delta}$ (1) and $Ce_{0.9}Y_{0.1}O_{2-\delta}-PrNi_{0.5}Co_{0.5}O_{3-\delta}$ (2) [45] samples sintered at 1100 °C. Points - experiment, lines - modeling.

Two distinct TPIE peaks are discernible in the YDC-PNC sample: the low-temperature peak corresponds to the substitution of oxygen in the YDC phase and YDC-PNC interfaces, while the high-temperature peak corresponds to the substitution of oxygen in the PNC phase.

Based on the data presented in Table 1, temperature dependences of the weighted average tracer diffusion coefficient (\bar{D}^*) values can be calculated according to Equation 1:

$$\bar{D}^* = \sum_i \theta_i D_i^* \exp\left(\frac{-E_i}{R} \left(\frac{1000}{T} - \frac{1000}{T_{REP}}\right)\right). \quad (1)$$

These \bar{D}^* values can be regarded as a generalized characteristic of the oxygen mobility in the samples. As an example, the temperature dependencies of \bar{D}^* for the samples sintered at 1100 °C are illustrated in Figure 15. The Bi-containing samples are observed to possess a high oxygen mobility at low temperatures.

Consequently, the findings of this study indicate that the samples containing bismuth exhibit a high degree of nonuniformity in oxygen mobility. This phenomenon is likely attributable to the unformed phase structure, resulting in elevated oxygen mobility at low temperatures. It is to be specially noted that there is a possible effect of the presence of the Bi_3YO_6 phase possessing a high oxygen mobility [62–64]; however, the oxygen transport properties may be strongly affected by a degree of the structural disorder, the presence of anionic defects and flexibility of the cationic framework. Moreover, the oxide anions neighboring to the Y cations may possess a lower oxygen mobility.

The oxide-ionic conductivity ($\sigma(O^{2-})$) for the samples can be estimated according to the Nernst-Einstein equation (Equation 2) [65]:

$$\sigma(O^{2-}) = H_R \frac{\bar{D}^* C(O^{2-}) (q(O^{2-}))^2}{k_B T}, \quad (2)$$

where H_R is the Haven ratio, \bar{D}^* is the average oxygen tracer diffusion coefficient calculated according to Equation 1, $C(O^{2-})$ and $q(O^{2-})$ are the concentration and charge of oxide anions, respectively, k_B is the Boltzmann constant, and T is the temperature. The estimated values of the oxide-ionic conductivity are $\sim 10^{-4}$ – 10^{-1} S/cm at 700 °C (Figure 16).

According to the phase composition, the composites of Bi cerates with YDC should be predominantly ionic conductors, while their composites with YDC and PNC should be mixed ionic-electronic conductors. A comparison of the oxide-ionic (Figure 16, curve 6) and total conductivity values (Figure 8, curve 2) for the BYC-YDC-PNC composite sintered at 1100 °C reveals the oxygen transport number values to be $\sim 3 \cdot 10^{-4}$ at 200–300 °C and $\sim 1 \cdot 10^{-4}$ at 400–600 °C, which is typical of mixed ionic-electronic conductors.

It is imperative to acknowledge the potential limitations of the estimations of oxide-ionic conductivity presented in Figure 16. These estimations may not accurately reflect the actual values due to the following reasons.

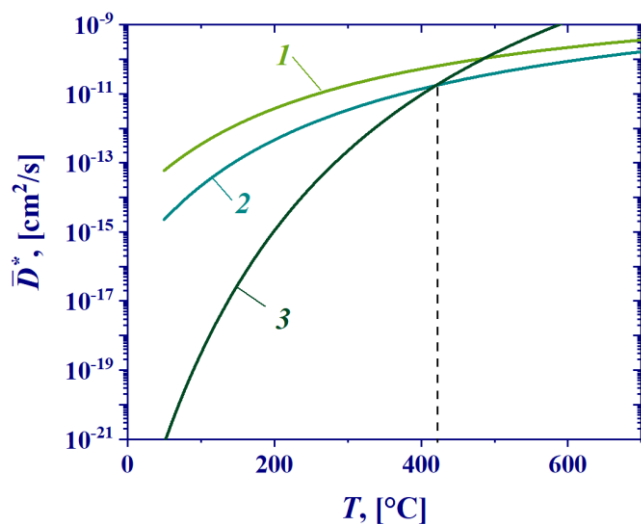


Figure 15 Temperature dependences of weighted average oxygen tracer diffusion coefficient for the $\text{Bi}_{1.6}\text{Y}_{0.4}\text{Ce}_2\text{O}_{7-\delta}\text{-Ce}_{0.9}\text{Y}_{0.1}\text{O}_{2-\delta}$ (1), $\text{Bi}_{1.6}\text{Y}_{0.4}\text{Ce}_2\text{O}_{7-\delta}\text{-Ce}_{0.9}\text{Y}_{0.1}\text{O}_{2-\delta}\text{-PrNi}_{0.5}\text{Co}_{0.5}\text{O}_{3-\delta}$ (2) and $\text{Ce}_{0.9}\text{Y}_{0.1}\text{O}_{2-\delta}\text{-PrNi}_{0.5}\text{Co}_{0.5}\text{O}_{3-\delta}$ (3) [42] samples sintered at 1100 °C according to the TPIE C^{18}O_2 data modeling.

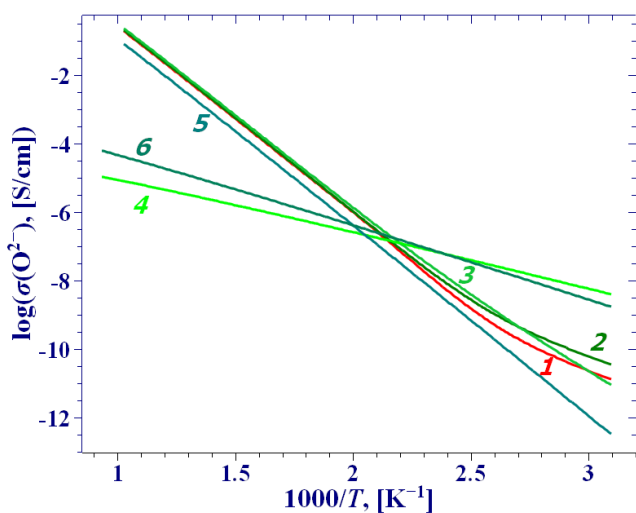


Figure 16 Temperature dependences of oxide-ionic conductivity estimated from the TPIE C^{18}O_2 data according to the Nernst-Einstein equation for the samples: (1) $\text{Bi}_2\text{Ce}_2\text{O}_{7-\delta}$ ($T_{\text{sint}} = 700$ °C), (2) $\text{Bi}_{1.6}\text{Y}_{0.4}\text{Ce}_2\text{O}_{7-\delta}$ (700 °C), (3) $\text{Bi}_2\text{Ce}_2\text{O}_{7-\delta}\text{-Ce}_{0.9}\text{Y}_{0.1}\text{O}_{2-\delta}$ (700 °C), (4) $\text{Bi}_2\text{Ce}_2\text{O}_{7-\delta}\text{-Ce}_{0.9}\text{Y}_{0.1}\text{O}_{2-\delta}$ (1100 °C), (5) $\text{Bi}_{1.6}\text{Y}_{0.4}\text{Ce}_2\text{O}_{7-\delta}\text{-Ce}_{0.9}\text{Y}_{0.1}\text{O}_{2-\delta}\text{-PrNi}_{0.5}\text{Co}_{0.5}\text{O}_{3-\delta}$ (700 °C), (6) $\text{Bi}_{1.6}\text{Y}_{0.4}\text{Ce}_2\text{O}_{7-\delta}\text{-Ce}_{0.9}\text{Y}_{0.1}\text{O}_{2-\delta}\text{-PrNi}_{0.5}\text{Co}_{0.5}\text{O}_{3-\delta}$ (1100 °C).

Firstly, the Haven ratio (H_R) is defined as the ratio of the oxygen diffusion coefficients determined from the isotope exchange and the conductivity measurement data. The H_R values in Equation 2 are assumed to be equal to 1. However, the H_R values may differ from 1 and be affected by the diffusion mechanism [66–68]. Secondly, the calculations do not take into account the correlation of transport of different oxygen forms; however, such a correlation may exist, and in this case the application of the Nernst-Einstein equation may result in the underestimation of the ionic conductivity values [69–72]. Finally, the effect of viscosity may lead to additional deviations from the Nernst-Einstein equation [72].

4. Limitations

The complex nature of the composite systems under investigation, as evidenced by the XRD data, makes thorough analysis of the experimental data acquired by such methods as electrochemical impedance spectroscopy and isotope exchange of oxygen sophisticated. The attribution of each oxygen form revealed by the isotope exchange of oxygen is hypothesized based on the existing literature data, including the authors' previous works. It is important to acknowledge the potential for alternative interpretations of the isotope exchange data. These include models that assume fast diffusion of the most mobile oxygen fraction, followed by slower exchange with neighboring, more strongly bound oxygen. Another possibility is taking into account the effective rate of mass transport between the solid and gas phases. It is also important to acknowledge that the estimation of oxide-ionic conductivity according to the Nernst-Einstein equation may not accurately reflect the real values due to the inherent limitations of the equation itself.

5. Conclusions

In this work, the composites based on $\text{Bi}_2\text{Ce}_2\text{O}_{7-\delta}$, $\text{Bi}_{1.6}\text{Y}_{0.4}\text{Ce}_2\text{O}_{7-\delta}$, $\text{Ce}_{0.9}\text{Y}_{0.1}\text{O}_{2-\delta}$ and $\text{PrNi}_{0.5}\text{Co}_{0.5}\text{O}_{3-\delta}$ were synthesized for the first time. For Bi cerate-based composites the pyrochlore phase transforms into the fluorite one after sintering at high temperatures, and various admixture phases are formed. The total conductivity is high enough for using these composites as oxygen separation membrane materials. The samples possess very high oxygen surface reactivity, which can be explained by the effect of oxygen vacancies, enhanced CO_2 adsorption of Bi-containing phases, and presence of highly defective surface layers. The oxygen diffusion exhibits a high degree of nonuniformity, probably due to unformed phase structure, the features of phase composition and real/defect structure, which results in formation of various oxygen forms and provides a high oxygen mobility even at low temperatures. The values of oxygen tracer diffusion coefficient of the most mobile oxygen ($\sim 10^{-6}$ cm^2/s at 700 °C) are comparable to or even exceed those for the state-of-the-art mixed ionic-electronic conductive materials such as Sr-doped Ba ferrites-cobaltites, and are comparable to the values for Bi_2O_3 , well-known fast oxygen conductor. Hence, the composites synthesized and studied in this work can be recommended for using as a component of the oxygen separation membranes.

Supplementary materials

No supplementary materials are available.

Data availability statement

Data will be made available on request.

Acknowledgments

None.

Author contributions

Conceptualization: E.S., V.S., Y.B.
 Data curation: E.S., T.K., Y.B.
 Formal Analysis: N.E., A.I., A.U.
 Investigation: N.E., S.M., T.K., A.I., A.U., Y.B.
 Methodology: E.S., V.S., Y.B.
 Project administration: V.S.
 Supervision: V.S., Y.B.
 Visualization: N.E., E.S., T.K., A.I., A.U., Y.B.
 Writing – original draft: N.E., S.M., E.S., T.K., Y.B.
 Writing – review & editing: V.S.

Conflict of interest

The authors declare no conflict of interest.

Additional information

Author IDs:

Nikita Eremeev, Scopus ID [55645818400](#);
 Ekaterina Sadovskaya, Scopus ID [57202034821](#);
 Tamara Krieger, Scopus ID [8233294600](#), [57216503916](#);
 Arcady Ishchenko, Scopus ID [57194264619](#);
 Artyom Ulikhin, Scopus ID [15046088200](#);
 Vladislav Sadykov, Scopus ID [7006677003](#);
 Yulia Bepalko, Scopus ID [36450050400](#).

Websites:

Federal Research Center Boreskov Institute of Catalysis SB
 RAS <https://en.catalysis.ru/>;
 Institute of Solid State Chemistry and Mechanochemistry SB
 RAS <http://www.solid.nsc.ru/en/>.

References

- Chen G, Widenmeyer M, Yu X, Han N, Tan X, Homm G, Liu S, Weidenkaff A. Perspectives on achievements and challenges of oxygen transport dual-functional membrane reactors. *J Am Ceram Soc.* 2024;107(3):1490–504. doi:[10.1111/jace.19411](#)
- Ji Liu J, Zhao J, Liu Y, Zhu Y, Zhou W, Gu Z, Zhang G, Liu Z. Research progress of computational fluid dynamics in mixed ionic–electronic conducting oxygen-permeable membranes. *Membranes.* 2025;15(7):193. doi:[10.3390/membranes15070193](#)
- Gao S, Song Z, Sun H, Zhang Y, Ma J, Zhang Y. Progress of oxygen generation technologies in high-altitude and emergency rescue conditions. *Asia-Pac J Chem Eng.* 2025;20(4):e70040. doi:[10.1002/apj.70040](#)
- Singh R, Prasad B, Ahn YH. Recent developments in gas separation membranes enhancing the performance of oxygen and nitrogen separation: A comprehensive review. *Gas Sci Eng.* 2024;123:205256. doi:[10.1016/j.jgsce.2024.205256](#)
- Casadio S, Gondolini A, Mercadelli E, Sanson A. Advances and prospects in manufacturing of ceramic oxygen and hydrogen separation membranes. *Renew Sustain Energy Rev.* 2024;200:114600. doi:[10.1016/j.rser.2024.114600](#)
- Bharatee RK, Quaff AR, Jaiswal SK. Advances in perovskite membranes for carbon capture & utilization: A sustainable approach to CO₂ emissions reduction – A review. *J Environ Manage.* 2025;380:124924. doi:[10.1016/j.jenvman.2025.124924](#)
- Porotnikova N, Osinkin D. Segregation and interdiffusion processes in perovskites: A review of recent advances. *J Mater Chem A.* 2024;12(5):2620–46. doi:[10.1039/D3TA06708D](#)
- Medvedev DA. Doping design strategies of proton-conducting perovskite oxides: A brief compositional map. *Int J Hydrogen Energy.* 2025;161:150689. doi:[10.1016/j.ijhydene.2025.150689](#)
- Lei S, Wang A, Xue J, Wang H. Catalytic ceramic oxygen ionic conducting membrane reactors for ethylene production. *React Chem Eng.* 2021;6(8):1327–41. doi:[10.1039/D1RE00136A](#)
- Zhu X, Yang W. Microstructural and interfacial designs of oxygen-permeable membranes for oxygen separation and reaction–separation coupling. *Adv Mater.* 2019;31(50):1902547. doi:[10.1002/adma.201902547](#)
- Shlyakhtina AV, Shcherbakova LG. New solid electrolytes of the pyrochlore family. *Russ J Electrochem.* 2012;48(1):1–25. doi:[10.1134/S1023193512010144](#)
- Kharton VV, Tsipis EV, Yaremchenko AA, Vyshatko NP, Shaula AL, Naumovich EN, Frade JR. Oxygen ionic and electronic transport in Gd_{2-x}Ca_xTi₂O_{7-δ} pyrochlores. *J Solid State Electrochem.* 2003;7(8):468–76. doi:[10.1007/s10008-002-0348-6](#)
- Dergacheva PE, Kul'bakin IV, Ashmarin AA, Titov DD, Fedorov SV. Bi_{1.4}Er_{0.6}Ru₂O_{7-50 wt % δ-Bi₂O₃} oxygen-permeable membrane material prepared by crystallization from partially molten state. *Russ J Inorg Chem.* 2021;66(8):1229–33. doi:[10.1134/S0036023621080040](#)
- Piir I, Koroleva M, Krasnov A. Electrochemical properties of complex pyrochlores. In: *Pyrochlore Ceramics.* Elsevier; 2022. pp. 243–75. doi:[10.1016/B978-0-323-90483-4.00006-4](#)
- Baratov S, Filonova E, Ivanova A, Hanif MB, Irshad M, Khan MZ, Motola M, Rauf S, Medvedev D. Current and further trajectories in designing functional materials for solid oxide electrochemical cells: A review of other reviews. *J Energy Chem.* 2024;94:302–31. doi:[10.1016/j.jechem.2024.02.047](#)
- Bukhari M, Mohsin M, Kayani ZN, Rasool S, Raza R. The La⁺³-, Nd⁺³-, Bi⁺³-doped ceria as mixed conductor materials for conventional and single-component solid oxide fuel cells. *Energies.* 2023;16(14):5308. doi:[10.3390/en16145308](#)
- Thangamuthu P, Moorthy S, Maria Mahimai B, Kannaiyan D, Deivanayagam P. High performance bismuth oxide embedded sulfonated poly ether sulfone composite membranes for fuel cell applications. *J Macromol Sci. A* 2023;60(3):171–80. doi:[10.1080/10601325.2023.2186793](#)
- Emhjellen LK, Xing W, Li Z, Haugsrud R. Oxygen permeability and surface kinetics of composite oxygen transport membranes based on stabilized δ-Bi₂O₃. *J Membr Sci.* 2022;660:120875. doi:[10.1016/j.memsci.2022.120875](#)
- Li ZC, Zhang H, Bergman B. Synthesis and characterization of nanostructured Bi₂O₃-doped cerium oxides fabricated by PVA polymerization process. *Ceram Int.* 2008;34(8):1949–53. doi:[10.1016/j.ceramint.2007.07.018](#)
- Cui B, Li Y, Li S, Xia Y, Zheng Z, Liu Y-Q. Bi-doped ceria as a highly efficient catalyst for soot combustion: Improved mobility of lattice oxygen in Ce_xBi_{1-x}O_y catalysts. *Energy Fuels.* 2020;34(8):9932–39. doi:[10.1021/acs.energyfuels.0c01090](#)
- Accardo G, Audasso E, Yoon SP. Unravelling the synergistic effect on ionic transport and sintering temperature of nanocrystalline CeO₂ tri-doped with Li Bi and Gd as dense electrolyte for solid oxide fuel cells. *J Alloys Compd.* 2022;898:162880. doi:[10.1016/j.jallcom.2021.162880](#)
- Anantharaman AP, Prasad Dasari H. Potential of pyrochlore structure materials in solid oxide fuel cell applications. *Ceram Int.* 2021;47(4):4367–88. doi:[10.1016/j.ceramint.2020.10.012](#)
- Wilde PJ, Catlow CRA. Defects and diffusion in pyrochlore structured oxides. *Solid State Ionics.* 1998;112(3–4):173–83. doi:[10.1016/S0167-2738\(98\)00190-8](#)
- Pirzada M, Grimes RW, Minervini L, Maguire JF, Sickafus KE. Oxygen migration in A₂B₂O₇ pyrochlores. *Solid State Ionics.* 2001;140(3–4):201–8. doi:[10.1016/S0167-2738\(00\)00836-5](#)
- Matsumoto U, Ogawa T, Fisher CAJ, Kitaoka S, Tanaka I. Cooperative oxide-ion transport in pyrochlore Y₂Ti₂O₇: A first-principles molecular dynamics study. *J Phys Chem C.* 2021;125(37):20460–7. doi:[10.1021/acs.jpcc.1c03610](#)
- Shlyakhtina AV, Belov DA, Knotko AV, Avdeev M, Kolbanov IV, Vorobieva GA, Karyagina OK, Shcherbakova LG. Oxide ion transport in (Nd_{2-x}Zr_x)Zr₂O_{7+δ} electrolytes by an interstitial mechanism. *J Alloys Compd.* 2014;603:274–81. doi:[10.1016/j.jallcom.2014.03.068](#)

27. Shlyakhtina AV Morphotropy, isomorphism, and polymorphism of $Ln_2M_2O_7$ -based ($Ln = La-Lu, Y, Sc; M = Ti, Zr, Hf, Sn$) oxides. *Crystalllogr Rep.* 2013;58(4):548–62. doi:[10.1134/S1063774513020259](https://doi.org/10.1134/S1063774513020259)
28. Perriot R, Dholabhai PP, Uberuaga BP. Disorder-induced transition from grain boundary to bulk dominated ionic diffusion in pyrochlores. *Nanoscale.* 2017;9(20):6826–36. doi:[10.1039/c7nr01373f](https://doi.org/10.1039/c7nr01373f)
29. Gupta AK, Arora G, Aidhy DS, Sachan R. $\Sigma 3$ twin boundaries in $Gd_2Ti_2O_7$ pyrochlore: Pathways for oxygen migration. *ACS Appl Mater Interfaces.* 2020;12(40):45558–63. doi:[10.1021/acsami.0c12250](https://doi.org/10.1021/acsami.0c12250)
30. Huo D, Baldinozzi G, Siméone D, Khodja H, Surlblé S. Grain size-dependent electrical properties of $La_{1.95}Sr_{0.05}Zr_{2}O_{7-\delta}$ as potential proton ceramic fuel cell electrolyte. *Solid State Ionics.* 2016;298:35–43. doi:[10.1016/j.ssi.2016.10.019](https://doi.org/10.1016/j.ssi.2016.10.019)
31. Shannon RD. Revised effective ionic radii and systematic studies of interatomic distances in halides and chalcogenides. *Acta Crystallogr.* 1976;32(5):751–67. doi:[10.1107/S0567739476001551](https://doi.org/10.1107/S0567739476001551)
32. Minervini L, Grimes RW, Sickafus KE. Disorder in pyrochlore oxides. *J Am Ceram Soc.* 2000;83(8):1873–8. doi:[10.1111/j.1151-2916.2000.tb01484.x](https://doi.org/10.1111/j.1151-2916.2000.tb01484.x)
33. Huang K, Feng M, Goodenough JB. Bi_2O_3 - Y_2O_3 - CeO_2 solid solution oxide-ion electrolyte. *Solid State Ionics.* 1996;89(1–2):17–24. doi:[10.1016/0167-2738\(96\)00260-3](https://doi.org/10.1016/0167-2738(96)00260-3)
34. Pesaran A, Jaiswal A, Ren Y, Wachsmann ED. Development of a new ceria/yttria-ceria double-doped bismuth oxide bilayer electrolyte low-temperature SOFC with higher stability. *Ionics.* 2019;25(7):3153–64. doi:[10.1007/s11581-019-02838-4](https://doi.org/10.1007/s11581-019-02838-4)
35. Uniyal S, Atri S, Uma S, Nagarajan R. Microstructural changes caused by Ba and Pr doping in nanosized $Bi_2Ce_2O_7$ leading to interesting optical, magnetic, and catalytic property. *CrystEngComm.* 2021;3(4):986–99. doi:[10.1039/DoCE01550D](https://doi.org/10.1039/DoCE01550D)
36. Li G, Mao Y, Li L, Feng S, Wang M, Yao X. Solid solubility and transport properties of nanocrystalline $(CeO_2)_{1-x}(BiO_{1.5})_x$ by hydrothermal conditions. *Chem Mater.* 1999;11(5):1259–66. doi:[10.1021/cm9806735](https://doi.org/10.1021/cm9806735)
37. Accardo G, Spiridigliozzi L, Dell'Agli G, Yoon SP, Frattini S. Morphology and structural stability of bismuth-gadolinium co-doped ceria electrolyte nanopowders. *Inorg.* 2019;7(10):118. doi:[10.3390/inorganics7100118](https://doi.org/10.3390/inorganics7100118)
38. Bepalko Yu, Ereemeev N, Sadovskaya E, Krieger T, Bulavchenko O, Suprun E, Mikhailenko M, Korobeynikov M, Sadykov V. Synthesis and oxygen mobility of bismuth cerates and titanates with pyrochlore structure. *Membranes.* 2023;13(6):598. doi:[10.3390/membranes13060598](https://doi.org/10.3390/membranes13060598)
39. Sadykov VA, Pavlova SN, Kharlamova TS, Muzykantov VS, Uvarov NF, Okhlupin YuS, Ishchenko AV, Bobin AS, Mezentseva NV, Alikina GM, Lukashevich AI, Krieger TA, Larina TV, Bulgakov NN, Tapilin VM, Belyaev VD, Sadovskaya EM, Boronin AI, Sobyenin VA, Bobrenok OF, Smirnova AL, Smorygo OL, Kilner JA. Perovskites and their nanocomposites with fluorite-like oxides as materials for solid oxide fuel cells cathodes and oxygen-conducting membranes: Mobility and reactivity of the surface/bulk oxygen as a key factor of their performance. In: *Perovskites: Structure, Properties and Uses.* New York: Nova Science Publishers, Inc.; 2010. pp. 67–178.
40. Sadykov V, Ereemeev N, Sadovskaya E, Bepalko Yu, Simonov M, Arapova A, Smal E. Nanomaterials with oxygen mobility for catalysts of biofuels transformation into syngas, SOFC and oxygen/hydrogen separation membranes: Design and performance. *Catal Today.* 2023;423:113936. doi:[10.1016/j.cattod.2022.10.018](https://doi.org/10.1016/j.cattod.2022.10.018)
41. Sadykov VA, Ereemeev NF, Sadovskaya EM, Bobin AS, Fedorova YuE, Muzykantov VS, Mezentseva NV, Alikina GM, Krieger TA, Belyaev VD, Rogov VA, Ulikhin AS, Okhlupin YuS, Uvarov NF, Bobrenok OF, McDonald N, Watton J, Dhir A, Steinberger-Wilckens R, Mertens J, Vinke IC. Cathodic materials for intermediate-temperature solid oxide fuel cells based on praseodymium nickelates-cobaltites. *Russ J Electrochem.* 2014;50(7):669–79. doi:[10.1134/S1023193514070131](https://doi.org/10.1134/S1023193514070131)
42. Stoyanovskii VO, Vedyagin AA, Volodin AM, Bepalko YuN. Effect of carbon shell on stabilization of single-phase lanthanum and praseodymium hexaaluminates prepared by a modified Pechini method. *Ceram Int.* 2020;46(18A):29150–9. doi:[10.1016/j.ceramint.2020.08.088](https://doi.org/10.1016/j.ceramint.2020.08.088)
43. Sadykov V, Pikalova E, Sadovskaya E, Shlyakhtina A, Filonova E, Ereemeev N. Design of mixed ionic-electronic materials for permselective membranes and solid oxide fuel cells based on their oxygen and hydrogen mobility. *Membranes.* 2023;13(8):698. doi:[10.3390/membranes13080698](https://doi.org/10.3390/membranes13080698)
44. Sadykov V, Sadovskaya E, Ereemeev N, Kolchugin A, Filonova E, Tsvinkinberg V, Zhulanova T, Pikalova E. Novel materials based on Ruddlesden-Popper phases for solid oxide fuel cells and oxygen separation membranes: Fundamentals of oxygen transport. *Chim Tech Acta.* 2025;12(3):12304. doi:[10.15826/chimtech.2025.12.3.04](https://doi.org/10.15826/chimtech.2025.12.3.04)
45. Sadykov VA, Sadovskaya EM, Uvarov NF. Methods of isotopic relaxations for estimation of oxygen diffusion coefficients in solid electrolytes and materials with mixed ionic-electronic conductivity. *Russ J Electrochem.* 2015;51(5):458–67. doi:[10.1134/S1023193515050109](https://doi.org/10.1134/S1023193515050109)
46. De Souza RA. Limits to the rate of oxygen transport in mixed-conducting oxides. *J Mater Chem A.* 2017;5(38):20334–50. doi:[10.1039/C7TA04266C](https://doi.org/10.1039/C7TA04266C)
47. Farver JR. Oxygen and hydrogen diffusion in minerals. *Rev Mineral Geochem.* 2010;72(1):447–507. doi:[10.2138/rmg.2010.72.10](https://doi.org/10.2138/rmg.2010.72.10)
48. Chronos A, Goulatis IL, Solovjov A, Vovk RV. The evolution of solid oxide fuel cell materials. *Appl Sci.* 2024;14(1):69. doi:[10.3390/app14010069](https://doi.org/10.3390/app14010069)
49. Klyndyuk AI, Chizhova EA, Kharytonau DS, Medvedev DA. Layered oxygen-deficient double perovskites as promising cathode materials for solid oxide fuel cells. *Mater.* 2022;15(1):141. doi:[10.3390/ma15010141](https://doi.org/10.3390/ma15010141)
50. Aidhy DS, Weber WJ. Microstructure design for fast oxygen conduction. *J Mater Res.* 2016;34(1):2–16. doi:[10.1557/jmr.2015.327](https://doi.org/10.1557/jmr.2015.327)
51. Goel P, Gupta MK, Mittal R, Skinner SJ, Mukhopadhyay S, Rols S, Chaplot SL. Phonons and oxygen diffusion in Bi_2O_3 and $(Bi_{0.7}Y_{0.3})_2O_3$. *J Phys Condens Matter.* 2020;32(33):334002. doi:[10.1088/1361-648X/ab88f8](https://doi.org/10.1088/1361-648X/ab88f8)
52. Bayliss RD, Cook SN, Kotsantonis S, Chater RJ, Kilner JA. Oxygen ion diffusion and surface exchange properties of the α - and δ -phases of Bi_2O_3 . *Adv Energy Mater.* 2014;4(10):1301575. doi:[10.1002/aenm.201301575](https://doi.org/10.1002/aenm.201301575)
53. Sadykov V, Shlyakhtina A, Sadovskaya E, Ereemeev N, Skazka V, Goncharov V. 2D diffusion of oxygen in $Ln_{10}Mo_2O_{21}$ ($Ln = Nd, Ho$) oxides. *Solid State Ionics.* 2020;346:115229. doi:[10.1016/j.ssi.2020.115229](https://doi.org/10.1016/j.ssi.2020.115229)
54. Sadykov V, Shlyakhtina A, Lyskov N, Sadovskaya E, Cherepanova S, Ereemeev N, Skazka V, Goncharov V, Kharytonova E. Oxygen diffusion in Mg-doped Sm and Gd zirconates with pyrochlore structure. *Ionics.* 2020;26(9):4621–33. doi:[10.1007/s11581-020-03614-5](https://doi.org/10.1007/s11581-020-03614-5)
55. Ereemeev NF, Bepalko YuN, Sadovskaya EM, Skriabin PI, Krieger TA, Ishchenko AV, Sadykov VA. Structural and transport properties of Nd tungstates and their composites with $Ni_{0.5}Cu_{0.5}O$ obtained by mechanical activation. *Dalton Trans.* 2022;51(19):7705–14. doi:[10.1039/d2dt00498d](https://doi.org/10.1039/d2dt00498d)
56. Raj AKV, Prabhakara Rao P, Sreena TS, Aju Thara TR. Pigmentary colors from yellow to red in $Bi_2Ce_2O_7$ by rare earth ion substitutions as possible high NIR reflecting pigments. *Dyes Pigment.* 2019;160:177–87. doi:[10.1016/j.dyepig.2018.08.010](https://doi.org/10.1016/j.dyepig.2018.08.010)
57. Pikalova E, Sadykov V, Tsvinkinberg V, Kolchugin A, Zhulanova T, Guseva E, Ereemeev N, Sadovskaya E, Belyaev V, Filonova E. Boosting the oxygen transport kinetics and functional properties of $La_2NiO_{4+\delta}$ via partial La-to-Sm substitution. *J Alloys Compd.* 2024;980:173648. doi:[10.1016/j.jallcom.2024.173648](https://doi.org/10.1016/j.jallcom.2024.173648)

58. Sadykov VA, Sadovskaya EM, Pikalova EYu, Kolchugin AA, Filonova EA, Pikalov SM, Ereemeev NF, Ishchenko AV, Lukashevich AI, Bassat JM. Transport features in layered nickelates: Correlation between structure, oxygen diffusion, electrical and electrochemical properties. *Ionics*. 2018;24(4):1181–93. doi:[10.1007/s11581-017-2279-3](https://doi.org/10.1007/s11581-017-2279-3)
59. Wang L, Merkle R, Maier J, Acartürk T, Starke U. Oxygen tracer diffusion in dense $\text{Ba}_{0.5}\text{Sr}_{0.5}\text{Co}_{0.8}\text{Fe}_{0.2}\text{O}_{3-\delta}$ films. *Appl Phys Lett*. 2009;94(7):071908. doi:[10.1063/1.3085969](https://doi.org/10.1063/1.3085969)
60. Liu Y, Wang M, Shen M, Wang Q, Zhang L. Bi-doped ceria with increased oxygen vacancy for enhanced CO_2 photoreduction performance. *J Inorg Mater*. 2021;36(1):88–94. doi:[10.15541/jim20200142](https://doi.org/10.15541/jim20200142)
61. Sadykov VA, Pavlova SN, Vinokurov ZS, Shmakov AN, Ereemeev NF, Fedorova YuE, Yakimchuk EP, Kriventsov VV, Bolotov VA, Tanashev YuYu, Sadovskaya EM, Cherepanova SV, Zolotarev KV. Application of SR methods for the study of nanocomposite materials for hydrogen energy. *Phys Procedia*. 2016;84:397–406. doi:[10.1016/j.phpro.2016.11.068](https://doi.org/10.1016/j.phpro.2016.11.068)
62. Krynski M, Wrobel W, Dygas JR, Wrobel J, Malys M, Śpiewak P, Kurzydowski KJ, Krok F, Abrahams I. *Ab-initio* molecular dynamics simulation of $\delta\text{-Bi}_3\text{YO}_6$. *Solid State Ionics*. 2013;245–6:43–8. doi:[10.1016/j.ssi.2013.05.015](https://doi.org/10.1016/j.ssi.2013.05.015)
63. Asif SU, Wang J, Qian Y, Gao D, Bashir R, Bilal MK, Ahmad J, Qadeer Awan M, Hu W. Phonon vibrations and photoluminescence emissions and their correlations with the electrical properties in Er^{3+} doped Bi_3YO_6 oxide-ion conductors. *Solid State Ionics*. 2020;344:115092. doi:[10.1016/j.ssi.2019.115092](https://doi.org/10.1016/j.ssi.2019.115092)
64. Krynski M, Wrobel W, Mohn CE, Dygas JR, Malys M, Krok F, Abrahams I. Trapping of oxide ions in $\delta\text{-Bi}_3\text{YO}_6$. *Solid State Ionics*. 2014;264:49–53. doi:[10.1016/j.ssi.2014.06.019](https://doi.org/10.1016/j.ssi.2014.06.019)
65. Murch GE. The Nernst–Einstein equation in high-defect-content solids. *Philos Mag A* 1982;45(4):685–92. doi:[10.1080/01418618208236198](https://doi.org/10.1080/01418618208236198)
66. Murch GE. The Haven Ratio in fast ionic conductors. *Solid State Ionics*. 1982;7(3):177–98. doi:[10.1016/0167-2738\(82\)90050-9](https://doi.org/10.1016/0167-2738(82)90050-9)
67. Akbar SA. A generalized view of the correlation factor in solid-state diffusion. *J Appl Phys*. 1994;75(6):2851–6. doi:[10.1063/1.356178](https://doi.org/10.1063/1.356178)
68. Poirier DR, Geiger GH. Fick's law and diffusivity of materials. In: *Transport Phenomena in Materials Processing*. Springer, Cham; 2016. pp. 419–61. doi:[10.1007/978-3-319-48090-9_12](https://doi.org/10.1007/978-3-319-48090-9_12)
69. Sasaki R, Tateyama Y, Searles DJ. Constant-current nonequilibrium molecular dynamics approach for accelerated computation of ionic conductivity including ion-ion correlation. *PRX Energy*. 2025;4:013005. doi:[10.1103/PRXEnergy.4.013005](https://doi.org/10.1103/PRXEnergy.4.013005)
70. Pang M-C, Marinescu M, Wang H, Offer G. Mechanical behaviour of inorganic solid-state batteries: Can we model the ionic mobility in the electrolyte with Nernst–Einstein's relation? *Phys Chem Chem Phys*. 2023;23(48):27159–70. doi:[10.1039/D1CP00909E](https://doi.org/10.1039/D1CP00909E)
71. De Souza RA. Oxygen diffusion in SrTiO_3 and related perovskite oxides. *Adv Funct Mater*. 2015;25(40):6326–42. doi:[10.1002/adfm.201500827](https://doi.org/10.1002/adfm.201500827)
72. Shao Y, Shigenobu K, Watanabe M, Zhang C. Role of viscosity in deviations from the Nernst–Einstein relation. *J Phys Chem B*. 2020;124(23):4774–80. doi:[10.1021/acs.jpcc.0c02544](https://doi.org/10.1021/acs.jpcc.0c02544)